https://dx.doi.org/10.1016/j.joule.2021.05.015

Unravelling the mechanical origin of stable solid electrolyte interphase

Yao Gao [a], Xiaoqiong Du [a], Zhen Hou [a], Xi Shen [b], Yiu-Wing Mai [c], Jean-Marie Tarascon [d], Biao Zhang [a,*]

[a] Department of Applied Physics, the Hong Kong Polytechnic University, Hung Hom, Kowloon, Hong Kong, China. Email: biao.ap.zhang@polyu.edu.hk

[b] Department of Mechanical and Aerospace Engineering, the Hong Kong University of Science and Technology, Clear Water Bay, Kowloon, Hong Kong, China

[c] Centre for Advanced Materials Technology (CAMT), School of Aerospace, Mechanical and Mechatronics Engineering J07, The University of Sydney, NSW 2006, Australia

[d] Chimie du Solide-Energie, UMR 8260, Collège de France, Paris, France

Abstract:

The capability of a solid electrolyte interphase (SEI) in accommodating the deformation is crucial to the electrode's integrity. However, SEI has a rather complicated microstructure with nanoscale thickness, making it challenging to characterize multiple mechanical parameters and identify the appropriate predictors for such capability. Here, we develop a feasible atomic force microscopy-based nanoindentation test that circumvent the interference of substrate, hence allowing to accurately probe the Young's modulus and the elastic strain limit of the SEI. The "*maximum elastic deformation energy* (*U*)" that that an SEI can absorb, which encompasses the collective effect of the above two metrics is proposed to predict the stability of the SEI as successfully demonstrated in Li/K metal anodes. We show that another asset of U is to provide a rapid and effective mean to screen proper electrolytes for enabling the stabilization of micro-sized Sn and Sb anodes through building high-U SEIs. Overall, this new indicator U offers future directions towards the rational design of robust SEIs for advanced anodes.

Introduction

The development of a stable solid electrolyte interphase (SEI) holds the key to successful commercialization of Li-ion batteries (LIBs)[1]. A SEI layer is formed on the anode surface because of the electrolyte reduction during the first cycle. This layer allows the diffusion of Li ions but blocks the electron transfer to prevent further decomposition on subsequent cycling.[2,3] The mechanical failure of SEI due to the repeated volume expansion of the anode leads to a continuous consumption of the electrolyte and hence a rapid decay in capacity, which is among the greatest challenges in developing metal and alloy anodes that experience large volume expansions. This challenge spans essentially to all existing and future battery chemistries and become more acute with the upcoming Na- and K- ones and mainly suffers the lack of an appropriate indicator to determine the capability against deformation.

To improve the mechanical properties of the SEI, many researchers have designed various approaches to tailor its microstructure which has significantly improved the cyclic stability of the electrodes.[4-10] Nonetheless, the correlation between the enhanced battery performance and the mechanical properties of the SEI remains unclear. Hence our motivation is to target the specific mechanical property of SEI so as to efficiently boost the cycling performance of batteries. Among the various mechanical properties, the Young's modulus and elastic strain limit are most widely examined.[10-15] It is generally accepted that a SEI with a high Young's modulus (E) enhances the cyclic performance.[16-19] On the contrast, several studies also indicate that the SEI having a large elastic strain limit (ε_Y) favors highly reversible batteries despite its low E.[3,20-22] Generally, it is difficult to find a material that reunites both a high Young's modulus and a large elastic strain limit. Finding

the proper trade-off between these two parameters is becoming essential to regulate the mechanical property of SEI; however, we are missing explicit theoretical guidelines.

More critically, the SEI has a rather complex chemical composition and nanoscale microstructure and is sensitive to electron beams and air.[23,24] These features make the precise mechanical characterization of the SEI a challenging task. Most studies on SEI mechanics adopt the atomic force microscopy (AFM)-based nanoindentation test,[10,12,23,25-27] which is simpler, more efficient, and reproducible than the tensile test of free-standing SEIs. Since the thickness of SEI is on the same scale as the penetration depth of the indentation test, the elastic field under the probe is not limited to the SEI itself but also extends to the underlying anode.[28] As such, the mechanical response of SEI/anode in the nanoindentation test is more reminiscent of a coating/substrate system rather than a bulk material. Ignoring the substrate effect could lead to inaccurate test results. Surprisingly, heretofore, the effect of the underlying anode on the evaluation of SEI's mechanical properties has not been reported.

In this work, we deviate from the classical approach relying on monitoring individual values of E and ε_Y, and propose to use the maximum elastic deformation energy (U) that an SEI can absorb to predict its stability during cycling. We optimize the AFM-based nanoindentation test by conducting two consecutive tests at the same position of the SEI to separately determine its elastic and plastic properties. The interference due to the anode is eliminated by adopting a coating/substrate model. The reliability of U in predicting the stability of the SEI during cycling is verified in both K and Li metal battery systems. We then construct SEIs having high U to stabilize the K-Sb and Li-Sn anodes, which validates the benefit of the proposed predictor U in screening promising electrolytes.

Clarifying the stress state of the SEI during charge/discharge cycles is the first step in unraveling the mechanical origin of stable SEI. To demonstrate our concept, we focus on the high-capacity metal and alloy anodes such as Sn or Sb, which suffer from severe volume expansion (nearly ~ 300%) during cycling. In metal anodes, such as Li and K, the ions diffuse through the SEI and deposit on the current collector (Fig. 1a, b). Having a confocal uniform and smooth deposition is a coveted goal but it is difficult to achieve in most cases. Under the internal pressure due to the battery encapsulation, the non-uniformly deposited atom clusters/islands (in metal anodes, Fig. 1b) or the electrochemically driven swelling of electrode particles (in alloy anodes, Fig. 1c, d) subject the SEI to a stress state akin to local indentations (inset of Fig. 1e).

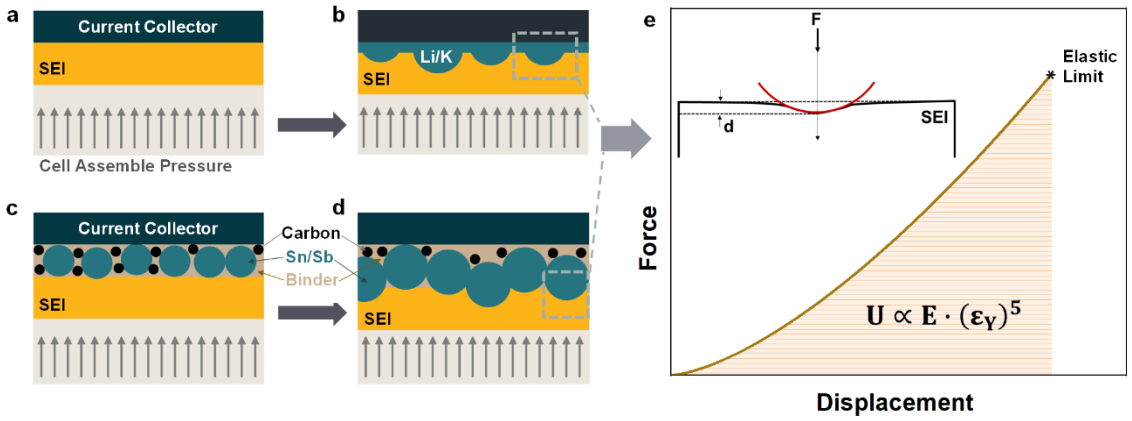

Figure 1. Stress state of the SEI during cycles: Illustrations of (a) (c) charged and (b) (d) discharged states of metal and alloy anodes; (e) A representative force-displacement curve for the Hertz contact model, with the inset being the stress state of the SEI over charge/discharge cycles.

In principle, either a larger E or ε_Y helps to resist or accommodate elastic deformation and favors uniform swelling[18,19], and therefore contributes to the stability of the SEI. However, the introduction of a parameter that could reflect the collective effects of E and ε_Y will be more than welcome in broadly addressing the SEI mechanical stability. We herein propose to use the "*maximum elastic deformation energy*" (U) a SEI can store

to predict its stability. The value of *U* corresponds to the area under the force-displacement (*F*-*d*) curve up to the elastic limit (Fig. 1e, see SI for derivation details):

$$U = \frac{8}{15}\left(\frac{4}{5}\pi\right)^5 \cdot r^3 \cdot (1-\nu^2)^4 \cdot E \cdot (\varepsilon_Y)^5, \quad (1)$$

where ν is the SEI's Poisson's ratio and *r* is the radius of the rigid indenter and assumed the same (ν = 0.3, *r* = 1 μm) for all systems. In practice, values of *E* and ε_Y of the SEI are obtained from AFM-based nanoindentation tests (Fig. 2a, b) in which the anode material is always bonded as a substrate to the SEI (because it is impossible to obtain a stand-alone SEI for testing). Hence, the effect of the substrate must be removed.

We develop a two-step nanoindentation test with the AFM to characterize separately both the Young's modulus and elastic strain limit of the SEI. They are performed at the same position on the surface of the SEI. The results are usually plotted as the force (*F*) vs displacement (*d*) curves with two segments, showing the approach and retract process of the indenter. The first indentation is conducted with a small force (~ 30 nN) such that the deformation of the SEI is limited to the elastic region, as evidenced by the coinciding "approach" and "retract" curves (Fig. 2a). The Young's modulus of the SEI is then evaluated by best fitting the unloading curve to the Hertz contact model (Eq. S1-S2)[29] taking into account the effect of the underlying anodes (see detailed discussion later). In the subsequent indentation, a larger loading (~ 900 nN) is applied to intentionally fail the SEI and then to obtain data on its elastic strain limit. A representative force-displacement curve is shown in Fig. 2b. Point (b) of the approach curve is located at the first discontinuity point corresponding to dislocation nucleation and plastic yielding[30], which is used to determine the elastic strain limit (ε_Y) of the SEI. The detailed derivation can be found in

Eq. S3-S10.[31] For each electrode sample, a total of more than 100 test positions are indented for calculations of the Young's modulus and the elastic strain limit.

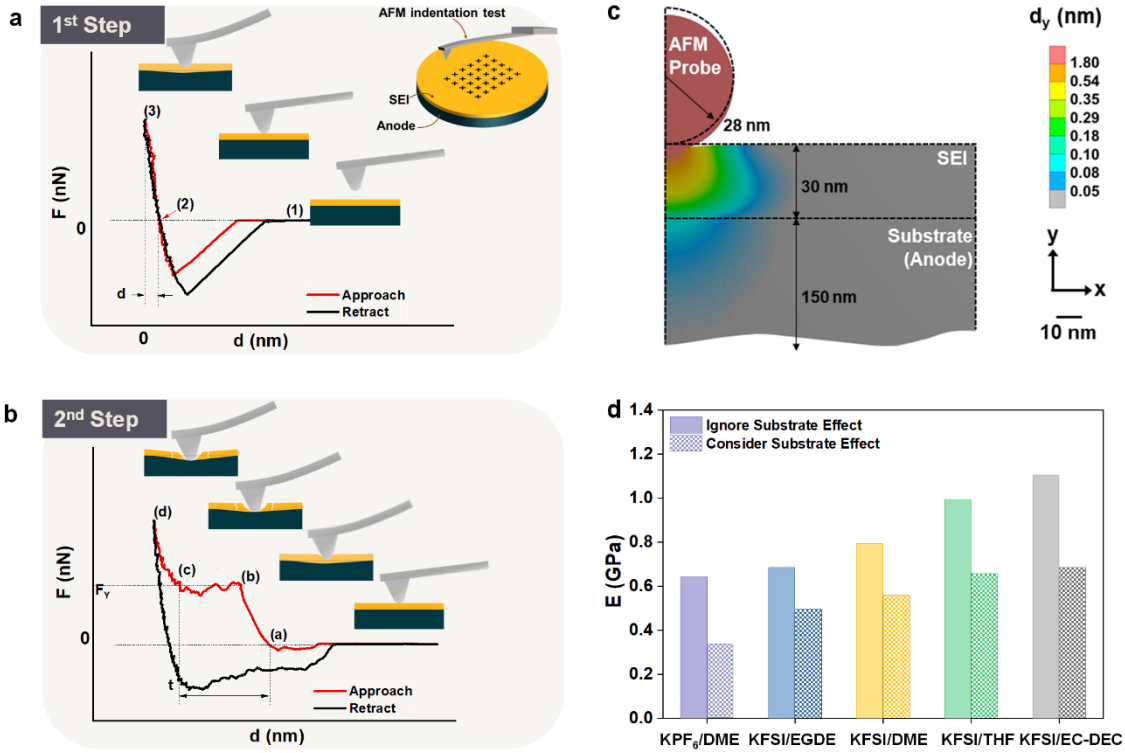

Figure 2. Probing the mechanical properties of SEI: Typical force-displacement curves obtained in the (a) first and (b) second step of the AFM-based nanoindentation test. The insets illustrate different stages during indentation corresponding to different positions in the force-displacement curves. Schematic diagram of AFM-based nanoindentation test of SEI which is bonded to the anode surface is illustrated in the inset of (a). (c) Deformation distribution of a SEI/anode system during the indentation process from FE simulations. The Young's moduli of SEI and anode are set to 500 MPa and 3.53 GPa, respectively, with an indentation depth of 3 nm. (d) Young's modulus of SEI formed on potassium metal anodes in five different electrolyte systems.

The anode materials beneath the SEI that are generally harder and much thicker than the SEI itself, serve as a substrate during indentation[32,33] (inset of Fig. 2a). We thus conduct finite element (FE) simulations (with ANSYS) to explore the substrate effects in extracting the Young's moduli from the nanoindentation tests (see SI for simulation details).

Fig. 2c displays one typical FE simulation result, where the indentation depth (d) is one-tenth the SEI thickness (t = 30 nm). Referring to the legend of Fig. 2c, the displacement degree of each point is indicated by their color. The deformed region extends beyond the SEI to the substrate, demonstrating clearly the non-negligible effect of the substrate. Fig. S1c summaries the FE simulation results and illustrates that omission of the substrate effect from the mechanics analysis significantly overestimates E by up to 200%. Such an over-estimation exacerbates with increasing indentation depth and widening difference between E and E_s (that is the Young's modulus of substrate). For a soft coating on a hard substrate, it is generally accepted that the substrate interference on hardness evaluation can be ignored when $d/t < 0.1$.[32,33] Our FE simulation results, however, show that the substrate has a more severe effect on the measurement of Young's modulus. Even when $d/t = 0.05$, ignoring the substrate effect leads to a 50% overestimation of E when $E/E_s = 0.014$, and a ~30% overestimation when $E/E_s = 0.57$. These results stress further that the substrate influence must be considered to accurately probe the Young's modulus of the SEI using indentation.

Bearing in mind the effect of the substrate, the Young's modulus of the SEI, E, is determined from the recast equation [28,34,35]:

$$E_r = \left[\frac{1-\nu_{tip}{}^2}{E_{tip}} + \frac{1-\nu^2}{E}\left(1-e^{-\frac{\alpha t}{a}}\right) + \frac{1-\nu_s{}^2}{E_s}\left(e^{-\frac{\alpha t}{a}}\right)\right]^{-1} \quad (2)$$

in which E_r is the reduced modulus determined by fitting the unloading curve of the first AFM test to the Hertz contact model (Eq. S1); ν_{tip}, ν_s and ν are the Poisson's ratios of AFM probe, substrate and SEI, respectively; E_{tip} and E_s are Young's moduli of the AFM probe and substrate, respectively; R is the radius of AFM probe; a ($= \sqrt{\pi R d}$) is the square root of the projected contact area; and α is a scaling parameter depending on a/t (Fig. S2 and Eq.

S11). The values of *d* and *t* are directly obtained from the force-displacement curves of the first and the second AFM tests, respectively, as marked in Fig. 2a and Fig. 2b.

Equation 2 is next used to experimentally probe the effect of the substrate on the modulus evaluation of SEI in K metal anodes. Cu/K cells are fabricated using Cu and K metal as the working and counter electrodes, respectively, where K is reversibly plated/stripped on Cu. SEI layers for mechanical characterization are in the discharged state after ten times of cycling in a wide variety of common electrolytes, including 1 M KPF_6/ethylene glycol dimethyl ether (DME), 1 M KFSI/ethylene glycol diethyl ether (EGDE), 1 M KFSI/DME, 1 M KFSI/tetrahydrofuran (THF) and 1 M KFSI/ethylene carbonate (EC) - diethyl carbonate (DEC). The corresponding Young's moduli of the SEI layers obtained with and without considering the substrate effect are plotted in Fig. 2d. Regardless of the electrolytes, the Young's moduli of the SEIs are overestimated by 41% to 97% when the substrate effect is ignored.

Having determined the correct Young's moduli and elastic strain limits of SEI layers we next search for a possible correlation between the mechanical properties and the stability of the SEI. Figure S3 compares the Coulombic efficiency (CE) of the K metal anode in the above five electrolytes as a function of cycle number. For the five samples, the CE values are below 96% in the first cycle as a result of the SEI formation. Afterwards, such an SEI prevents the continuous consumption of electrolytes, leading to augmented CEs with cycling for all systems. The CE eventually reaches 99.15%, 98.88%, 98.57%, 94.24% and 68.89% in the 10^{th} cycle for 1 M KFSI/EGDE, 1 M KFSI/DME, 1 M KFSI/THF, 1 M KFSI/EC-DEC and 1 M KPF_6/DME systems, respectively (Fig. S3). This is in agreement with Xiao et al.'s[36] previous work which reports the benefit of ether-(DME)

over carbonate-based electrolyte for improving the electrochemical performance of K metal batteries. Moreover, we observe that EGDE with a different linear ether structure from DME and THF with a cyclic ether structure also deliver promising performances. In addition, SEIs formed in the first three systems display no obvious variation in their CEs over more than 100 cycles while those in the last two systems fall quickly in the first 50 cycles. Thus, we use the average Coulombic efficiency (ACE) in the first 50 cycles to characterize the stability of the SEI.

To interrogate a possible correlation between the two mechanical parameters and the ACE, we construct (Fig. 3a) the ε_Y-E diagram within which each electrolyte is positioned with their respective ACE. The SEI in 1M KFSI/EC-DEC electrolyte having the highest E (xx Mpa) amongst the five (Fig. 2d) shows an inferior performance than its counterparts having lower E (Fig. S3 and 3a). Shortly, there is no significant correlation between ACE and the individual values of ε_Y or E. In contrast, we observe that, the stable systems are located in the upper right region of the ε_Y-E diagram. This indicates that the maximum elastic deformation energy (U, defined in Eq. 1) could be a compelling indicator to represent the SEI's stability since it embodies the synergistic effect of ε_Y and E.

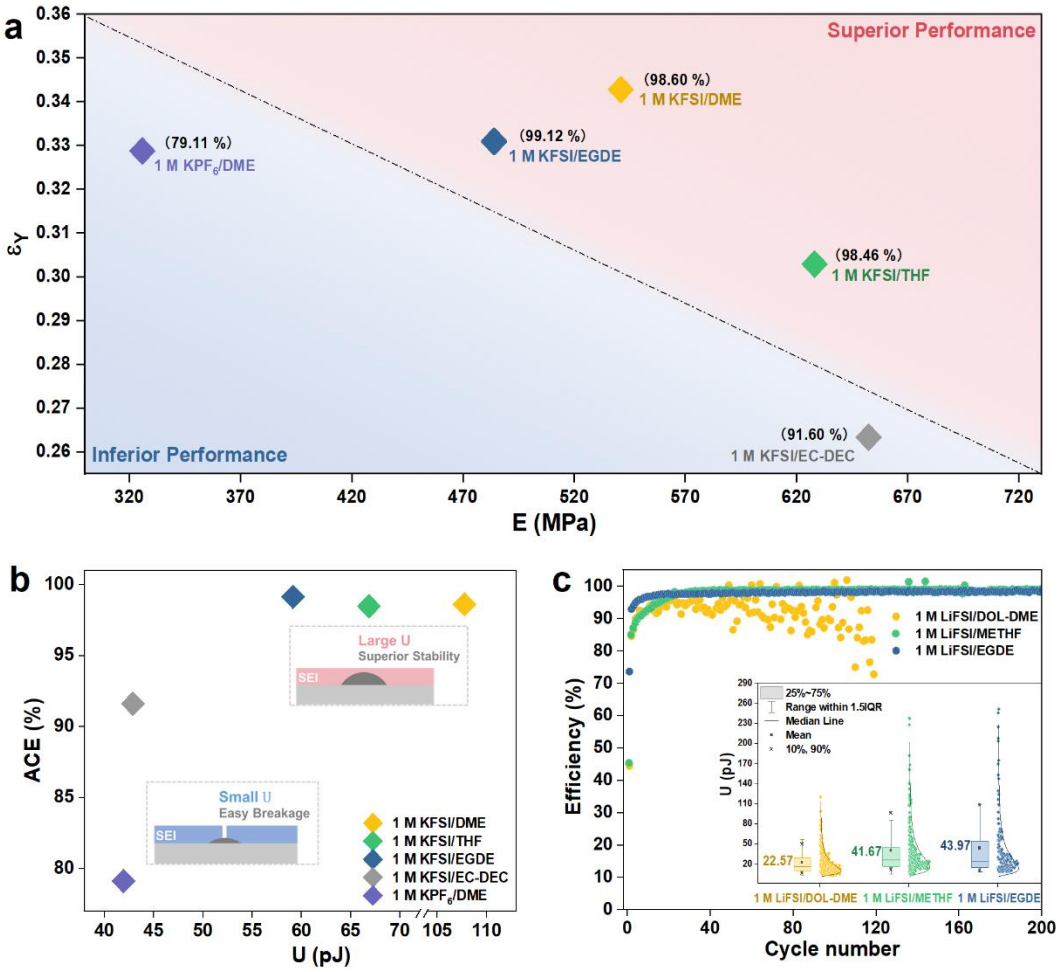

Figure 3. Function of the maximum elastic deformation energy *U*: (a) Plot of elastic strain limit against Young's modulus of the SEIs. Values in the parentheses indicate the ACE of corresponding SEI. (b) The relationship between the ACE and *U* of SEIs. The insets are illustrations of stable/unstable SEIs. (c) Cyclic performance of lithium metal anodes. The inset is *U* for SEIs formed in different electrolytes (sample size: $N_{DOL\text{-}DME}$=157, N_{METHF}=208, N_{EGDE}=205).

Further exploiting this direction, we plot the ACE against *U* in Fig. 3b and observe a pronounced correlation between the two parameters. The *U* values of SEIs in the two poorly cycling systems are only about 70% of that in 1 M KFSI/EGDE. This is because a SEI having a low *U* is not able to absorb all the energy generated during the K-plating process so that extra energy is consumed through the breakage of SEI, resulting in a low CE. Raising the *U* value significantly increases the maximum energy the SEI can sustain, such that all energy is absorbed by elastic deformation of the SEI without failure, leading to drastically improved CE as demonstrated in the 1 M KFSI/EGDE system. It should be

mentioned that the capacity loss between each plating/stripping includes (i) potassium ions consumed in forming new SEI (SEI-related) and (ii) inactive potassium due to the loss of electrical contact (non-SEI related)[37]. Building an SEI with a large elastic energy is crucial in preventing the SEI-related capacity loss but cannot guarantee a 100% CE. This explains why the ACE does not show a clear improvement when *U* is further increased in the cases of 1 M KFSI/THF and 1 M KFSI/DME, where the non-SEI related capacity loss dominates the ACE.

We further extend our study to Li metal anode to investigate if such an indicator *U* can be generalized to other systems. Similarly, Cu/Li half cells are fabricated in three electrolytes, i.e., 1 M LiFSI/1,3-dioxolane (DOL)-DME, 1 M LiFSI/2-Methyltetrahydrofuran (METHF) and 1 M LiFSI/EGDE (Fig. 3c and Fig. S4), and the corresponding SEIs after ten cycles are investigated. Neither of the individual parameter *E* nor ε_Y exhibits a clear correlation with battery performance (Fig. S5). However, similar to the case of K metal anodes, there is a nice correlation between the maximum elastic deformation energy *U* of the SEIs formed in these electrolyte systems and their corresponding ACEs (Fig. 3c inset), further strengthening the robustness of our correlation. The newly developed electrolyte, 1 M LiFSI/EGDE, yields the highest ACE due to the largest *U* (43.97 pJ) of the resulting SEI. By contrast, an inferior performance is observed in the widely adopted 1 M LiFSI/DOL-DME electrolyte owing to the feeble SEI with a *U* value (22.57 pJ) only half of its EGDE counterpart. These results confirm that the maximum elastic deformation energy *U* is effective to indicate the stability of the SEI. Compared to the two individual parameters of *E* and ε_Y used to represent the SEI's capabilities to either resist or buffer elastic deformation, the indicator *U* which relies on the combined effects of these two parameters stands as a new metric of the SEI stability.

For completeness of this work, we decide to demonstrate the real benefit of our finding for the improvement of anodes such as alloy anodes, e.g., Si, Sn and Sb. These anodes possess superior capacity in alkali-metal ion batteries, but their practical applications are still plagued by the electrode pulverization and repeated SEI failure/formation upon cycling due to the large volume expansion. For proof of concept we will here use Sn and Sb. A substantial amount of work has already been devoted to the

nanostructure design of electrodes to alleviate the internal stress, but none of the approaches are fully satisfactory yet. It is thus tempting to implement our strategy that consists in creating high-*U* SEIs for K-Sb and Li-Sn anodes via electrolyte chemistry regulation.

Let us first recall that Sb anode delivers an exceptional theoretical capacity of 660 mAh g^{-1} in K ion batteries, but it undergoes fast capacity fading in a classic carbonate electrolyte, i.e., 1 M KFSI/EC-PC (Fig. 4a and Fig. S6). The reason lies partly in the mechanically weak SEI that cannot buffer the K-driven deformation, hence the need to explore the possible electrolyte formula to fabricate high-*U* SEI. We examine the U of SEI formed on the Sb anode after three cycles in different electrolytes and find that the one in 1 M KFSI/THF electrolyte has a promising *U* value of 84.28 pJ, which is more than two times that in a classic carbonate electrolyte (*U*=34.29 pJ) (Fig. 4b). Consequently, the Sb anode can be stably cycled for 100 times in 1 M KFSI/THF with a sustainable capacity of 460 mAh g^{-1} at 0.5 A g^{-1}. By contrast, the 1 M KFSI/EC-PC electrolyte fails to stabilize the Sb anode and the cell capacity is significantly degraded after 20 cycles (Fig. 4a).

Now regarding the Li-Sn anode, that has a theoretical specific capacity of 994 mAh g^{-1}.[38] ,we find that it shows an excellent cyclic performance in the presence of an inert diluent 1,1,2,2-tetrafluoroethyl-2,2,3,3-tetrafluoropropylether (HFE)-DME-based electrolyte. Sn anodes show indeed a stable discharge capacity of ~685 mAh g^{-1} over 200 cycles in 1 M LiFSI/ DME-HFE at 0.3 A g^{-1}. (Fig. 4c and Fig. S8). By contrast, a rapid capacity fading is observed in 1 M LiFSI /EC-DMC. The *U*, *E* and ε_Y for the SEI in these two electrolytes obtained from the AFM-based nanoindentation tests are plotted in Fig. 4d and Fig. S9, respectively. The *U* value (71.76 pJ) of the SEI formed in 1 M LiFSI/DME-HFE electrolyte is twice of that formed in 1 M LiFSI/EC-DMC electrolyte (*U*=35.72 pJ), explaining the huge difference in their cycling performance. Hence, these results further validate the capability of high-*U* SEIs in accommodating the deformation, enabling the stabilization of micro-sized alloy anodes without resorting to the nanostructure design of the electrodes.

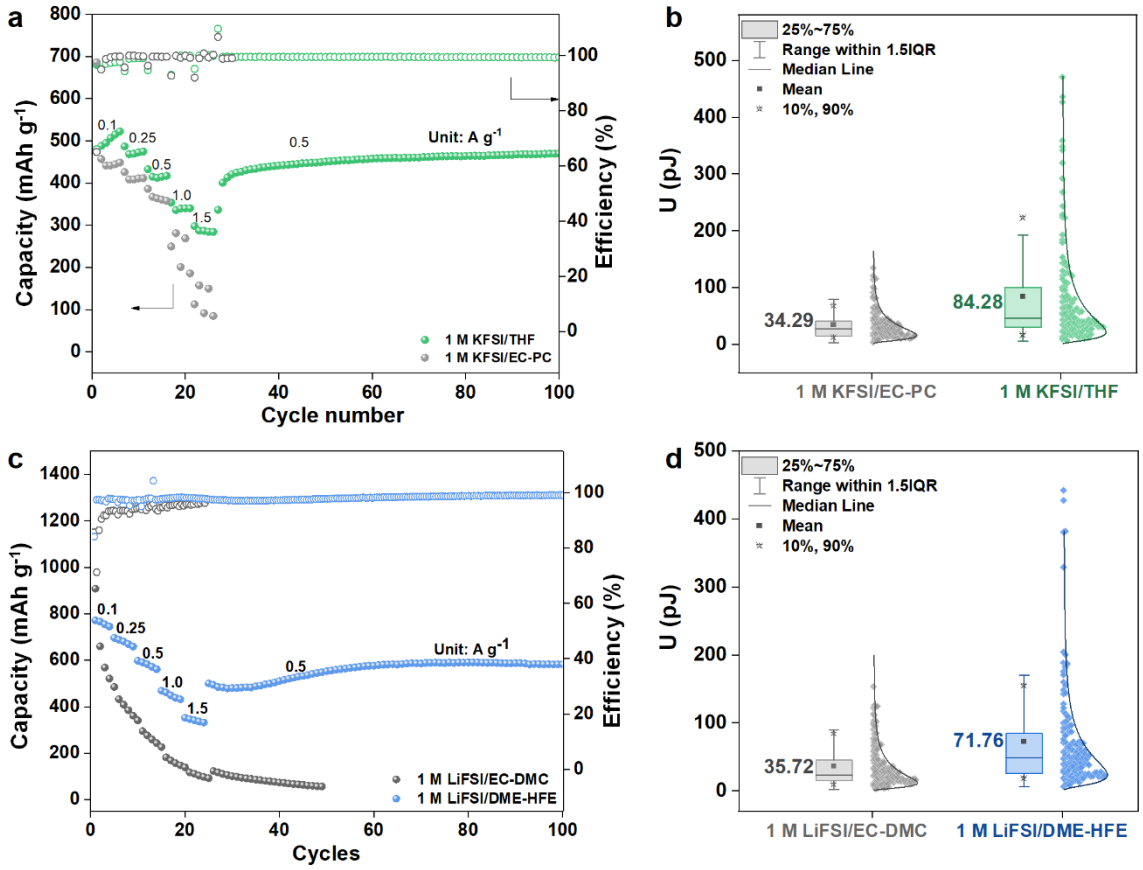

Figure 4. Performance of alloy anodes: Cyclic stability of (a) K-Sb and (c) Li-Sn anodes; and *U* values for SEIs formed on (b) Sb (sample size: $N_{EC\text{-}PC}$=115, N_{THF}=123) and (d) Sn electrodes (sample size: $N_{EC\text{-}DMC}$=165, $N_{DME\text{-}HFE}$=175) in different electrolytes.

At this stage a remaining pending question regards the underlying science to account for the formation of such high-*U* SEI. We analyse the chemical compositions of the SEI formed in the Li-Sn and K-Sb alloy anodes and find as usually reported in the literature that the SEI consists of both organic and inorganic species. The XPS results in Fig. S10 and Fig. S11 indicate the SEI in carbonate electrolytes has a much higher content of inorganic components, such as $ROCO_2Li(K)$ and Li_2CO_3, than that in ether-based electrolytes for the cases in both Li-Sn and K-Sb systems. The inorganic particles have much larger Young's moduli than the organic polymeric components whatever their exact formulation that resemble the polyethylene glycol polymer. We conduct FE simulations (using ANSYS) to explore the influence of inorganic particles on the maximum elastic

strain energy absorbed in the SEI loaded by a spherical indenter (see details in SI). The single organic phase model and two-phase model with a few and multiple inorganic particles (Fig. S12,13) are constructed. The simulation results (Fig. S14) show that the presence of inorganic particles greatly reduces the maximum elastic deformation energy of the SEI, and this reduction is enhanced with increasing content of inorganic particles. The large mismatch between the Young's moduli of the organic and inorganic phases causes stress concentrations at their interfaces, (Fig. S14), enabling the two-phase model to debond or yield more easily than the single-phase counterpart. These results are in good agreement with the fact that the *U*-values of the SEI formed in the carbonate-based electrolyte are smaller than those of the SEI formed in the ether-based electrolyte, because the former is more abundant in inorganic particles.

Collectively these observations suggest the strong dependence of *U* on the microstructure of the SEI, but also the detrimental effect of having interfaces with weak mechanical properties in achieving an SEI with high *U* value. We are well aware of the present model, applied to inorganic nanoparticles dispersed into an organic matrix is far to corner the complexity of the SEI, since multi-layered and inorganic dominated SEI has also been reported[39-41]. The maximum elastic deformation energy *U* would be controlled by the composition, phase morphology, amount of filler, matrix properties, and filler/matrix interface bonding. All this information could be obtained from knowledge in the field of nanocomposites[42]. Hence, further optimization of *U* relies on the resolution of the SEI's detailed structure through emerging techniques such as cryo-TEM[9,43,44], based on which the electrolyte formula could be optimized to tailor the SEI's microstructure.

Conclusion

We propose to use the "*maximum elastic deformation energy* (*U*)" as an effective indicator to represent the mechanical stability of a SEI during cycling. *U* embodies the combined impacts of *E* and ε_Y, which are comprehensively characterized by a two-step AFM-based nanoindentation test. Given the nanoscale thickness of the SEI, the coating/ substrate model is used to eliminate the interference of the underlying anode on evaluating the mechanical

properties. A high *U* allows the SEI to absorb all the energy imparted by anode swelling via elastic deformation, leaving no excessive energy to induce mechanical failure of the SEI and thus resulting in a drastically improved stability. The reliability of *U* in predicting the stability of the SEI during cycling is verified in both K and Li metal anodes.

The identification and accurate measurement of the mechanical predictor *U* of SEI stability greatly facilitates the screening of promising electrolytes, which is demonstrated in the alloy anodes. Assisted by the high-*U* SEI, stable cycling of Sn and Sb micro-particles is realized. Moreover, we also reveal that the usually low-*U* SEI formed in carbonate-based electrolytes probably results from the increased amount of mechanically weak interfaces between inorganic particles and polymer matrix. This work provides a strategic direction in rational microstructure design of robust SEIs to accommodate the deformation. It could pave the way towards the next generation of Li-ion batteries based on metal-alloys negative electrodes.

References

1 Choi, J. W. & Aurbach, D. Promise and reality of post-lithium-ion batteries with high energy densities. *Nature Reviews Materials* **1**, 1-16 (2016).

2 Liu, T. *et al.* In situ quantification of interphasial chemistry in Li-ion battery. *Nature nanotechnology* **14**, 50-56 (2019).

3 Li, S. *et al.* Developing high-performance lithium metal anode in liquid electrolytes: challenges and Progress. *Advanced Materials* **30**, 1706375 (2018).

4 Zhang, B. *et al.* Microsized Sn as advanced anodes in glyme-based electrolyte for Na-Ion batteries. *Advanced Materials* **28**, 9824-9830 (2016).

5 Wang, H. *et al.* Electrolyte Chemistry Enables Simultaneous Stabilization of Potassium Metal and Alloying Anode for Potassium-Ion Batteries. *Angewandte Chemie International Edition* **58**, 16451-16455 (2019).

6 Lei, Y. *et al.* Unveiling the influence of electrode/electrolyte interface on the capacity fading for typical graphite-based potassium-ion batteries. *Energy Storage Materials* **24**, 319-328 (2020).

7 Chen, J. *et al.* Electrolyte design for LiF-rich solid-electrolyte interfaces to enable high-performance microsized alloy anodes for batteries. *Nature Energy* **5**, 386-397 (2020).

8 Li, G. *et al.* Organosulfide-plasticized solid-electrolyte interphase layer enables stable lithium metal anodes for long-cycle lithium-sulfur batteries. *Nature Communications* **8**, 1-10 (2017).

9 Gao, Y. *et al.* Polymer–inorganic solid–electrolyte interphase for stable lithium metal batteries under lean electrolyte conditions. *Nature materials* **18**, 384-389 (2019).

10 Gu, Y. *et al.* Designable ultra-smooth ultra-thin solid-electrolyte interphases of three alkali metal anodes. *Nature communications* **9**, 1339 (2018).

11 Koerver, R. *et al.* Chemo-mechanical expansion of lithium electrode materials - on the route to mechanically optimized all-solid-state batteries. *Energy & Environmental Science* **11**, 2142-2158 (2018).

12 Kuznetsov, V. *et al.* Wet Nanoindentation of the Solid Electrolyte lnterphase on Thin. Film Si Electrodes. *Acs Applied Materials & Interfaces* **7**, 23554-23563 (2015).

13 Weadock, N. *et al.* Determination of mechanical properties of the SEI in sodium ion batteries via colloidal probe microscopy. *Nano Energy* **2**, 713-719 (2013).

14 Laresgoiti, I., Kaebitz, S., Ecker, M. & Sauer, D. U. Modeling mechanical degradation in lithium ion batteries during cycling: Solid electrolyte interphase fracture. *Journal of Power Sources* **300**, 112-122 (2015).

15 Müller, S. *et al.* Quantification and modeling of mechanical degradation in lithium-ion batteries based on nanoscale imaging. *Nature communications* **9**, 1-8 (2018).

16 Stone, G. *et al.* Resolution of the modulus versus adhesion dilemma in solid polymer electrolytes for rechargeable lithium metal batteries. *Journal of The Electrochemical Society* **159**, A222-A227 (2012).

17 Liu, Y. *et al.* An artificial solid electrolyte interphase with high Li-ion conductivity, mechanical strength, and flexibility for stable lithium metal anodes. *Advanced Materials* **29**, 1605531 (2017).

18 Monroe, C. & Newman, J. The effect of interfacial deformation on electrodeposition kinetics. *Journal of The Electrochemical Society* **151**, A880 (2004).

19 Monroe, C. & Newman, J. The impact of elastic deformation on deposition kinetics at lithium/polymer interfaces. *Journal of The Electrochemical Society* **152**, A396 (2005).

20 McGrogan, F. P. *et al.* Compliant Yet Brittle Mechanical Behavior of Li2S–P2S5 Lithium-Ion-Conducting Solid Electrolyte. *Advanced Energy Materials* **7**, 1602011 (2017).

21 Liu, K., Bai, P., Bazant, M. Z., Wang, C.-A. & Li, J. A soft non-porous separator and its effectiveness in stabilizing Li metal anodes cycling at 10 mA cm− 2 observed in situ in a capillary cell. *Journal of Materials Chemistry A* **5**, 4300-4307 (2017).

22 Suo, L. *et al.* Fluorine-donating electrolytes enable highly reversible 5-V-class Li metal batteries. *Proceedings of the National Academy of Sciences* **115**, 1156-1161 (2018).

23 Huang, J. *et al.* Nanostructures of solid electrolyte interphases and their consequences for microsized Sn anodes in sodium ion batteries. *Energy & Environmental Science* **12**, 1550-1557 (2019).

24 v. Cresce, A., Russell, S. M., Baker, D. R., Gaskell, K. J. & Xu, K. In Situ and Quantitative Characterization of Solid Electrolyte Interphases. *Nano letters* **14**, 1405-1412 (2014).

25 Zhang, J. *et al.* Direct observation of inhomogeneous solid electrolyte interphase on MnO anode with atomic force microscopy and spectroscopy. *Nano letters* **12**, 2153-2157 (2012).

26 Yoon, I., Jurng, S., Abraham, D. P., Lucht, B. L. & Guduru, P. R. In Situ Measurement of the Plane-Strain Modulus of the Solid Electrolyte Interphase on Lithium-Metal Anodes in Ionic Liquid Electrolytes. *Nano letters* **18**, 5752-5759 (2018).

27 Shin, H., Park, J., Han, S., Sastry, A. M. & Lu, W. Component-/structure-dependent elasticity of solid electrolyte interphase layer in Li-ion batteries: Experimental and computational studies. *Journal of Power Sources* **277**, 169-179 (2015).

28 Saha, R. & Nix, W. D. Effects of the substrate on the determination of thin film mechanical properties by nanoindentation. *Acta materialia* **50**, 23-38 (2002).

29 Hertz, H. On the contact of elastic solids. *Z. Reine Angew. Mathematik* **92**, 156-171 (1881).

30 Page, T. F. & Hainsworth, S. V. Using nanoindentation techniques for the characterization of coated systems: a critique. *Surface and Coatings Technology* **61**, 201-208 (1993).

31 Gao, Y., Shi, S.-Q. & Zhang, T.-Y. Adhesion contact deformation in nanobridge tests. *Nanoscale* **9**, 6033-6040 (2017).

32 Manika, I. & Maniks, J. Effect of substrate hardness and film structure on indentation depth criteria for film hardness testing. *Journal of Physics D: Applied Physics* **41**, 074010 (2008).

33 Westbrook, J. H. *The science of hardness testing and its research applications*. (American Society for Metals, Ohio, 1973).

34 Doerner, M. F. & Nix, W. D. A method for interpreting the data from depth-sensing indentation instruments. *Journal of Materials research* **1**, 601-609 (1986).

35 King, R. B. Elastic analysis of some punch problems for a layered medium. *Int. J. Solids Struct.* **23**, 1657-1664 (1987).

36 Xiao, N., McCulloch, W. D. & Wu, Y. Reversible dendrite-free potassium plating and stripping electrochemistry for potassium secondary batteries. *Journal of the American Chemical Society* **139**, 9475-9478 (2017).

37 Fang, C. *et al.* Quantifying inactive lithium in lithium metal batteries. *Nature* **572**, 511-515 (2019).

38 Ying, H. & Han, W. Q. Metallic Sn-Based Anode Materials: Application in High-Performance Lithium-Ion and Sodium-Ion Batteries. *Adv Sci (Weinh)* **4**, 1700298 (2017).

39 Chen, C. *et al.* Impact of dual-layer solid-electrolyte interphase inhomogeneities on early-stage defect formation in Si electrodes. *Nature Communications* **11**, 1-10 (2020).

40 Zhou, Y. *et al.* Real-time mass spectrometric characterization of the solid–electrolyte interphase of a lithium-ion battery. *Nature nanotechnology* **15**, 224-230 (2020).

41 Heiskanen, S. K., Kim, J. & Lucht, B. L. Generation and evolution of the solid electrolyte interphase of lithium-ion batteries. *Joule* **3**, 2322-2333 (2019).

42 Fu, S.-Y., Feng, X.-Q., Lauke, B. & Mai, Y.-W. Effects of particle size, particle/matrix interface adhesion and particle loading on mechanical properties of particulate–polymer composites. *J Composites Part B: Engineering* **39**, 933-961 (2008).

43 Li, Y. *et al.* Atomic structure of sensitive battery materials and interfaces revealed by cryo–electron microscopy. *Science* **358**, 506-510 (2017).

44 Shadike, Z. *et al.* Identification of LiH and nanocrystalline LiF in the solid–electrolyte interphase of lithium metal anodes. *Nature nanotechnology*, 1-6, 10.1038/s41565-020-00845-5 (2021).

Acknowledgements

This work was supported by the General Research Fund (GRF) scheme of the Hong Kong Research Grants Council (Projects No. 15305219, and 15301220), the Hong Kong

Polytechnic University (ZVGH), and Guangdong-HK-Macau Joint Lab on Solar-Thermo-Electro Materials and Device (ZGBQ).

Author contributions

Y.G., X.D., and Z.H. contributed equally to this work. B.Z. and Y.G. designed the research. Y.G., X.D., and Z.H. prepared and characterized the batteries. Y.G. conducted AFM-based mechanical tests and FE simulations. Y.G., X.D. and Z.H. optimized the electrolytes, conducted XPS and TEM characterizations. Y.G., X.D., Z.H., X.S., Y.M., J.M.T. and B.Z. analyzed the data, discussed the results and wrote the manuscript. All authors reviewed and contributed to the final manuscript.

Conflicts of interest

There are no conflicts to declare.

Additional Information

Supplementary information is available.

Methods

Anode preparation.

Sb anodes were prepared by mixing commercial Sb powders (Sigma-Aldrich, 300 mesh, 99.5%) with vapor-grown carbon fibers (VGCF), carbon black (Super P) and carboxymethyl cellulose (CMC) at a mass ratio of 7:1:1:1 to make a tape on Cu current

collector and dried at 80 ºC overnight under vacuum. Sn anodes were fabricated employing commercial Sn powders (Sigma-Aldrich, 10 μm, 99%) to replace Sb powders using the aforementioned procedure.

Electrolyte.

Electrolytes were prepared by dissolving the salts [(i) KFSI (Energy Chemical, purity 98%,), (ii) KPF_6 (Alfa Aesar, 99%); or (iii) LiFSI (DoDochem, purity 99.8%)] into the solvents [(i) EGDE (Sigma-Aldrich, 99%), DME (Sigma-Aldrich, 99.5%), THF (Alfa Aesar, 99%), EC (DoDochem, purity 99.95%)-DEC (DoDochem, purity 99.95%) with the volume ratio being 1:1; or (ii) EC-PC (DoDochem, purity 99.95%) with the volume ratio being 1:1; or (iii) DOL (DoDochem, purity 99.8%)-DME with the volume ratio being 1:1, METHF (Sigma-Aldrich, purity 99%); or (iv) EC-DMC (DoDochem, purity 99.8%) with the volume ratio being 1:1, DME-HFE (DoDochem) and the volume ratio of DME to HFE is 1:3] at a concentration of 1 M.

Battery assembly and electrochemical testing.

All batteries were assembled with the two-electrode CR2032 coin half-cell in an argon-filled glovebox (H_2O<0.5 ppm, O_2<0.5 ppm) and were tested on the LAND battery testing system. The potassium metal batteries were assembled with a K counter electrode and a bare Cu foil working electrode. The separator consists of a piece of polypropylene (Celgard) and a piece of glass fiber (Whatman, GF/D). The Li metal anode was tested in a similar structure but with the Li metal as the counter electrode. During the battery test, a fixed rate of 1 mA cm^{-2} or 3 mA cm^{-2} was used during cycling with a discharge time of 1 h and a

charge cutoff at 1.0 V (vs Li/Li^+ or K/K^+). The Sb and Sn anodes were examined against K and Li counter electrode, respectively, in coin cells with the glass fiber separator. 80 μL of electrolytes were used for each coin cell.

AFM-based nanoindentation test.

Mechanical tests using the Bruker Dimension Icon AFM (Bruker, Santa Barbara, CA) were conducted inside the glovebox. To improve the accuracy and reliability of the tests, a probe with an appropriate spring constant should be selected based on the range of target modulus values. For our case, the final identified probe was ACTA-20 (APPNANO) with a spring constant of 21.20 N m^{-1}. Before each test, the deflection sensitivity of the AFM cantilever was calibrated on a clean sapphire sample. The tip radius (R) was calibrated using reference samples (Polystyrene, Bruker PeakForce QNM Samples) with known elastic modulus. The calibration of the tip radius and spring constant was conducted before and after each indentation test to ensure the accuracy of data analysis. The test area was first scanned with an ultra-low set force of 2 nN to depict the surface morphology without introducing permanent changes to the sample. Using the "point and shoot" function of the AFM, over 100 positions in the scanned area were selected, and their positions were marked by "×". A gap of at least 200 nm was spaced between adjacent test positions to avoid interference with each other. The maximum force for the first test was set at 30 nN to obtain as many force-displacement data points as possible while maintaining the deformation of the SEI in the elastic region. In the second test, the maximum loading force was set to 900 nN to intentionally break the SEI and thus to obtain data on its elastic strain limit.

FE simulations of substrate effect.

During the FE simulation using ANSYS Workbench, a thin film (SEI) was bonded to a substrate and indented by the AFM probe under normal load and frictionless conditions. The AFM probe was simulated by a circle with a radius of 28 nm, which initially formed a tangential contact with the top surface of the SEI layer (Fig. S1a). The thicknesses of the SEI and the substrate were set as 30 nm and 150 nm, respectively. A fine mesh with an element size of 1.5 nm was applied to the likely contact region (centers at the initial contact site with a radius of 50 nm). Away from the contact region, relatively large mesh elements (element size: ~8 nm) were adopted. Moreover, a pinch-mesh was utilized at the interface between the SEI and the substrate. The element type of mesh is quadrilateral for all cases. In the FE simulations, the Young's modulus and Poisson's ratio of the substrate were fixed at 3.53 GPa and 0.35, respectively (values of potassium). Different values of E were applied to the SEI layer: 0.05 GPa, 0.2 GPa, 0.8 GPa, 1.4 GPa and 2.0 GPa. For each E value, FE simulations were conducted with five different indentation depth-to-thickness ratios ranged from 0.022 to 0.26. The SEI was set to behave as elastic-plastic with a maximum elastic strain of 0.1. The substrate was treated as a pure elastic material. A downward force was applied to the top center of the rigid ball with up to 200 sub-steps and the augmented Lagrange function was adopted in the computation.